This is a repository copy of *Single atom Cu(I) promoted mesoporous titanias for photocatalytic Methyl Orange depollution and H2 production*.

White Rose Research Online URL for this paper:
https://eprints.whiterose.ac.uk/129806/

Version: Accepted Version

**Article:**
Trofimovaite, Rima, Parlett, Christopher M.A., Kumar, Santosh et al. (8 more authors) (2018) Single atom Cu(I) promoted mesoporous titanias for photocatalytic Methyl Orange depollution and H2 production. APPLIED CATALYSIS B-ENVIRONMENTAL. pp. 501-511. ISSN 0926-3373

https://doi.org/10.1016/j.apcatb.2018.03.078

**Reuse**
This article is distributed under the terms of the Creative Commons Attribution-NonCommercial-NoDerivs (CC BY-NC-ND) licence. This licence only allows you to download this work and share it with others as long as you credit the authors, but you can't change the article in any way or use it commercially. More information and the full terms of the licence here: https://creativecommons.org/licenses/

**Takedown**
If you consider content in White Rose Research Online to be in breach of UK law, please notify us by emailing eprints@whiterose.ac.uk including the URL of the record and the reason for the withdrawal request.

eprints@whiterose.ac.uk
https://eprints.whiterose.ac.uk/

# Single atom Cu(I) promoted mesoporous titanias for photocatalytic Methyl Orange depollution and $H_2$ production

Rima Trofimovaite,[a] Christopher M. A. Parlett,[a] Santosh Kumar,[a] Lucia Frattini,[a] Mark A. Isaacs,[a] Karen Wilson,[d] Luca Olivi,[b] Ben Coulson,[c] Richard E. Douthwaite[c] and Adam F. Lee*[d]

[a]*European Bioenergy Research Institute, Aston University, Birmingham B4 7ET, UK.*

[b]*Sincrotrone Trieste, 34149 Basovizza, Trieste, Italy.*

[c]*Department of Chemistry, University of York, York YO10 5DD, UK.*

[d]*School of Science, RMIT University, Melbourne VIC 3000, Australia.*

## Abstract

Tailoring the physicochemical properties and hence reactivity of semiconductor photocatalysts in a predictable fashion, remains a challenge to their industrial application. Here we demonstrate the striking promotional effect of incorporating single Cu(I) atoms, on aqueous phase photocatalytic dye degradation and $H_2$ production over surfactant-templated mesoporous $TiO_2$. X-ray absorption spectroscopy reveals that ultra-low concentrations of copper (0.02-0.1 wt%) introduced into the mesoporous $TiO_2$ surface create isolated Cu (I) species which suppress charge recombination, and confer a six-fold photocatalytic promotion of Methyl Orange degradation and four-fold enhancement of $H_2$ evolution. The impact of mesopore structure and photophysical properties on photocatalytic activity is also quantified for the first time: calcination increases mesopore size and nanocrystalline order, and induces an anatase→rutile phase transition that is accompanied by a decrease in the optical band gap, increased charge carrier lifetime, and a concomitant significant activity enhancement.

Keywords: photocatalysis; titania; mesoporous; copper; XAS

## Introduction

Heterogeneous, semiconductor photocatalysts have received significant attention due to their potential application in diverse photoinduced reactions, notably solar fuels[1, 2] and hydrogen generation,[3] and wastewater and air depollution.[4] Titania has been widely used for water depollution[5] due to its abundance, low cost, thermochemical stability, low toxicity and suitable optical properties.[6] In this context, commercial P25 titania, comprising anatase and rutile crystallites (which appear to exhibit synergistic photocatalysis due to heterojunction formation) is typically the first

port of call for academic and industrial applications.[7, 8] However, P25 suffers from a low surface area (50 $m^2.g^{-1}$), wide band gap (restricting it to UV light absorption) and rapid recombination of photoexcited charge carriers.[9, 10] Consequently significant research efforts have focused on developing high area, thermally stable titanias with enhanced photophysical properties.

Antonelli et al[11] synthesised the first high internal surface area (200 $m^2.g^{-1}$), mesoporous $TiO_2$ with uniform (3.2 nm) pores via a modified sol-gel synthesis using titanium alkoxides and phosphate surfactants. High area (150-240 $m^2.g^{-1}$) and highly crystalline mesoporous titania microspheres with average pore diameters ~4.5 nm were more recently synthesised via evaporation induced self-assembly and acetic acid mediated sol-gel chemistries.[12] However, mesoporous $TiO_2$ catalysts with such mesopores are only amenable to substrates with small hydrodynamic diameters, and may suffer mass transport limitations for bulky molecules (such as azo dyes). Zhou et al[13] developed a lengthy, multi-step route to achieve larger (10 nm) well-ordered mesopores in anatase $TiO_2$, and investigated the thermal stability and photoactivity of this material for 2,4-dichlorophenol degradation. The highly crystalline anatase mesoporous $TiO_2$ exhibited better photocatalytic activity than P25, nonetheless, charge carrier separation was limited in this single phase material. In this latter example, it is surprising to note that calcination of disordered mesoporous titanias failed to induce any systematic variation in the anatase:rutile phase composition, or photoactivity for imazapyr or phenol decomposition.[14] Despite efforts to optimise the synthesis of mesoporous $TiO_2$ photocatalysts,[11-17] there remains no general route to systematically tune their phase or mesostructure.

Titania photoactivity is predominantly influenced by structural and electronic properties,[18, 19] which may be tuned via crystal structure engineering.[20] The commonly studied metastable anatase and stable rutile phases both exhibit wide band gaps (3.2 eV and 3.0 eV respectively)[21], with anatase-rich mixtures with rutile proposed optimal for MO degradation due to charge separation across their interface.[22, 23] Density functional calculations have also highlighted the importance of crystal facets for anatase, with surface energies and photoactivity of decreasing from (001) 0.90 J $m^{-2}$ > (100) 0.53 J $m^{-2}$ > (101) 0.44 J $m^{-2}$.[24, 25] Surface defects such as oxygen vacancies ($V_o$) and $Ti^{3+}$ sites also enhance $TiO_2$ photoactivity,[26] alongside particle size effects which dictate an optimum for 25-40 nm particles due to competition between light harvesting, scattering, bulk / surface recombination and geometric surface area.[27] Heterojunction formation[28] and doping[29] are promising approaches to overcome the limitations of pure titanias through modifying the quantum efficiency, band gap/energies, charge carrier mobility, surface structure, and adsorption properties.[23, 28-33] Functionalising by earth abundant metals such as copper is especially appealing with a wide range of promoter formats employed, including Cu metal,[34] $Cu_xO$ clusters,[35] nano-$Cu_2O$,[28] Cu doped sol-gels,[36, 37] $Cu(OH)_2$ clusters,[38] and $Cu_2O$ shells[39] to extend light absorption and improve charge carrier mobility, and in turn quantum efficiencies for photocatalytic pollutant degradation[28, 34-36] and solar fuels production.[38, 39] Cu-doped titania has also been exploited for thermo- and photocatalytic applications, including butene hydrogenation,[40] $CO_2$ reduction,[37] $H_2$ production,[41] and dye degradation.[42] In most cases, copper is introduced at moderate→high loadings spanning 0.5-5 wt% Cu, resulting in the formation of $Cu_2O$,[37, 42] CuO,[41] and/or Cu metal nanoparticles of 1-10 nm.[40]

However, it has proven difficult to unequivocally identify the copper oxidation state (due to XPS sensitivity and energy resolution limitations) or location of copper species (discrete particles or within the titania framework) for low loadings and highly dispersed particles.

Considering the former application, water pollution and its associated impact on human health accounts for >840,000 fatalities annually worldwide.[43] Around 80 % of contaminants in wastewater arise from the unregulated discharge of toxic, recalcitrant organic compounds by the textile, paper, petrochemical, food, energy and mineral processing sectors into aquatic ecosystems, and their depollution represents a significant challenge particularly for emerging countries.[44] Recalcitrant organic compounds, which include organic Azo dyes such as Methyl Orange, cannot be treated by conventional biological and/or physicochemical processing (e.g. microorganisms, flocculation or chlorination);[45, 46] the concentration of such Azo-dyes can reach 500 ppm in in textile effluent.[47] Advanced oxidation processes, including Fenton oxidation,[48] photocatalytic oxidation,[49, 50] photo-Fenton oxidation,[51] catalytic wet air oxidation,[52] electrocatalytic oxidation,[53] electro-Fenton oxidation[54] are promising solutions for the oxidative removal of persistent organic compounds from wastewater. However, while Fenton-type AOPs exhibit high removal efficiencies (100 mg/L) for diverse ROCs including cyanotoxins, they share a common high demand for $H_2O_2$ (~2.1 kg per kg of biological/chemical oxygen demand).[55] Furthermore, heterogeneous Fenton analogues are susceptible to transition metal leaching.[56] Hence, photocatalytic solutions to wastewater depollution are highly sought after.[4] In regard of the second application above, energy security and climate change represent key global challenges arising from historic reliance on fossil fuels.[57] Artificial photosynthesis offers the possibility of clean energy through water photolysis and renewable chemicals through $CO_2$ utilisation as a sustainable feedstock, commonly termed solar fuels and chemicals.[58] Hydrogen production through photocatalytic water splitting over semiconductor nanomaterials represents one of the most promising routes for the conversion and storage of solar energy in a form amenable for transportation.[59]

Here, we demonstrate the first synthetic route to high area, mesoporous $TiO_2$ with systematically tunable textural and photophysical properties, enabling facile control over their photocatalytic activity for both aqueous phase Methyl Orange degradation (in the absence of dye sensitisation) and hydrogen production. Post-functionalisation of mesoporous titania surfaces by ultra-low (0.1 wt%) concentrations of copper confers a six-fold enhancement in the rate of Methyl Orange photodegradation, and a four-fold increase in $H_2$ evolution, which Cu K-edge XAS reveal are associated with the genesis of atomically-dispersed Cu(I) species, and concomitant improvements in charge carrier lifetime. This work represents the first report that single Cu(I) atoms can promote titania photocatalysis, and quantitative correlation of the effect of titania mesoporosity on photocatalytic activity. The unexpected synergy between isolated Cu(I) atoms and mesoporous titania offers a new approach to promoted photocatalysts utilising earth abundant elements.

## Experimental

***Materials***

Titanium (IV) n-butoxide (ACROS Organics, 99.0 %), Pluronic F-127 (Sigma-Aldrich), nitric acid (Fisher, 70 %), ethanol (Fisher, analytical reagent grade), copper (II) nitrate trihydrate (ACROS Organics, 99 %), Methyl Orange (Sigma-Aldrich, Reag. Ph. Eur.), anatase (ACROS Organics, 98.0 %), rutile (Sigma-Aldrich, 99.99 %) and P25 (Sigma-Aldrich, 99.5 %) were used as received.

***Catalyst preparation***

Mesoporous titanias (meso-$TiO_2$-XC, X=calcination temperature) were synthesised through a surfactant templating route employing the non–ionic triblock copolymer Pluronic F-127 (12,600 g $mol^{-1}$, 7.7 g) dissolved in ethanol (120 ml), followed by $HNO_3$ (6.3 ml) and titanium (IV) n-butoxide (16 ml) addition under rapid stirring. The resulting solution was stirred at room temperature for 6 h, and then transferred to an oven for solvent evaporation at 50 °C for 18 h. The gel thus obtained was calcined in a muffle furnace at a range of temperatures between 300-700 °C (ramp rate of 1 °C.$min^{-1}$ in each case) for 4 h, and finally ground to a fine powder. Copper doped materials were prepared by subsequent wet impregnation of a Cu(II) nitrate trihydrate solution of variable concentration on the 500 °C calcined mesoporous $TiO_2$ (meso-$TiO_2$-500C) to achieve Cu loadings spanning 0.02 to 12.33 wt%. The aqueous slurry was stirred in the dark at 50 °C for 17 h until a dry powder was obtained, and the resulting solid subsequently re-calcined at 400 °C (ramp rate of 10 °C.$min^{-1}$) under flowing oxygen (10 ml.$min^{-1}$) for 2 h, and finally ground to a fine powder.

***Characterisation***

Nitrogen porosimetry was performed on Quantachrome NOVA 4000e and 4200e porosimeters with analysis by NovaWin v11.03 software. Samples were degassed at 120 °C in vacuo for 16 h before measurement. BET (Brunauer-Emmett-Teller) surface areas were calculated over the relative pressure range 0.05-0.35. Mesopore size distributions were estimated applying the BJH (Barrett-Joyner-Halenda) method to the desorption isotherm for relative pressures >0.35. Powder X-ray diffraction (XRD) patterns were recorded on a Bruker D8 ADVANCE diffractometer (40 kV, 40 mA) employing a Cu $K_\alpha$ (1.54 Å) source fitted with a LynxEYE high speed strip detector and calibrated against a corundum standard. Wide-angle patterns were recorded for 2θ=10-80° with 0.02° steps and low-angle patterns recorded for 2θ=0.3-8° in 0.01° steps. The proportion of crystalline anatase and rutile was estimated from the Spurr–Myers equation:

$\% \, Anatase = \frac{1}{1+1.265\frac{I_R}{I_A}} x100 \, \%$ ; $\% \, Rutile = \frac{1}{1+0.8\frac{I_A}{I_R}} x100\%$ where $I_R$ and $I_A$ are the respective peak height of the rutile (110) and anatase (101) reflections.[60, 61] Temperature-programmed oxidation (TPD) was conducted using a Mettler Toledo TGA-DSC 2 thermal analyser from 45-800 °C (ramp rate of 10 °C.$min^{-1}$) under flowing $N_2/O_2$ (40:20 v/v, total flow of 60 ml.$min^{-1}$). Diffuse reflectance UV-vis spectroscopy (DRUVS) was performed on a Thermo Scientific

Evolution 220 spectrophotometer equipped with an ISA-220 integrating sphere. Optical band gaps were determined from Tauc plots for an indirect band gap material, F(R)= $(\frac{(1-R)^2}{2R} \times h\upsilon)^{1/2}$ using the Kubelka-Munk formalism, where R corresponds to reflectance (%R/100), with the band gap obtained from the intersection of a tangent to the function with the energy axis. High-resolution scanning transmission electron microscopy (HR-STEM) images were recorded on a JEOL 2100F FEG microscope operating at 200 keV and equipped with a spherical aberration probe corrector (CEOS GmbH). Samples were prepared by dispersion in methanol and drop-casting onto a copper grid coated with a holey carbon support film (Agar Scientific). Images were analysed using ImageJ v1.46r software. X-ray absorption spectroscopy (XAS) measurements were undertaken at the XAFS beamline of the Elettra synchrotron. Ex-situ fluorescence and transmission Cu K-edge (8987.96 eV) spectra were acquired on powder samples diluted with BN and packed in Teflon washers. Spectra were normalised, background subtracted, and fitted to $Cu_2O$, CuO, $Cu(NO_3)$ and Cu foil standards using the Athena and Artemis components of the IFEFFIT software suite version 1.2.11d respectively. Time-resolved photoluminescence spectra of aqueous suspensions (1 $mg.mL^{-1}$) of samples were recorded on a F-4500FL spectrometer at an excitation wavelength of 380 nm.

***Photocatalytic activity***

Photocatalytic Methyl Orange (MO) degradation tests of meso- $TiO_2$ and Cu/meso-$TiO_2$ materials were performed in a sealed 150 ml quartz photoreactor (27 mm i.d.) maintained at an ambient of temperature 20°C through a recirculating cooling-jacket connected to a Huber Minichiller. 50 mg of catalyst was added to 50 ml of a 20 ppm MO aqueous solution stirred at 625 rpm in the dark for 1 h to establish an adsorption-desorption equilibrium prior to illumination. The reactor was subsequently irradiated (26 $mW.cm^{-2}$ reactor internal flux) under stirring by a 200 W Newport Oriel Instruments 66002 Hg Xe arc lamp employing a water filter to remove infrared wavelengths. Reaction aliquots were periodically withdrawn, centrifuged to remove catalyst, and analysed in cuvettes by UV-Vis absorption spectroscopy employing a Thermo Scientific Evolution 220 spectrophotometer. Initial degradation rates were calculated spectrophotometrically from the 464 nm MO absorption band, employing multi-point calibration curves and corrected for background rates of dye photolysis in the absence of catalyst. Degradation products were determined on periodically withdrawn and filtered aliquots using an Agilent 1200 series HPLC equipped with refractive index and UV diode array detectors, and a Zorbox Eclipse column and 10 % acetonitrile/90 % water mobile phase. For hydrogen production via water splitting, 50 mg of sample was dispersed in 50 ml of 0.5 M $Na_2SO_3$ aqueous solution (sulphite as a hole scavenger), and ultrasonicated for 10 min to obtain a uniform dispersion. Subsequently, the reaction mixture was purged with He (15 ml/min) for 1 h to remove air from the system. Aliquots of the reaction gas mixture was periodically withdrawn in both reactions to measure gas products with a 1 ml air-tight gas syringe for analysis on a Shimadzu Tracera GC-2010 Plus gas chromatography fitted with a Carboxen1010 (30 m × 0.53 mm × 0.1 μm) column with a He carrier gas and Barrier Ionization Detector. Values reported for both reactions are the mean of 3 repeats. Mass-normalised photocatalytic activities are reported in all cases since this is the only means to enable quantitative benchmarking of different catalysts: photocatalytic reactions, in

common with all types of catalytic reactions, must always be performed in regimes wherein the rate of reactant conversion is directly proportional to the catalyst mass; if this is not the case, then the activity observed may reflect e.g. mass transport kinetics or self-absorption, rather than intrinsic reaction kinetics of the catalyst. The masses of different photocatalysts should not be arbitrarily optimised (for example focusing solely on maximising product yield), since this prohibits fair comparison of their intrinsic performance.

## Results and discussion

### *Thermal evolution of mesoporous $TiO_2$*

A series of meso-$TiO_2$ materials was synthesised by a one-pot surfactant templating method and thermal processing at temperatures spanning 300 to 700 °C, and characterised by a range of structural and photophysical methods. Wide angle XRD diffractograms for all meso-$TiO_2$ materials (**Fig. 1**) exhibited reflections indexed to (101), (004), (200), (105,211), (204), (116,220) and (215) planes of anatase crystallites (PDF no. 21-1272).[62] Higher temperature calcination at 500-700 °C also induced additional reflections characteristic of a crystalline rutile phase (PDF no. 21-1276). The relative rutile:anatase peak intensity increased with calcination temperature (from 3 % to 15 % between 500-700 °C, **Table 1**) consistent with the greater thermodynamic stability of rutile. Crystallites sizes were estimated from the Scherrer equation and evidenced sintering of both anatase (from 5→31 nm) and rutile (from 29→46 nm) particles with increasing calcination temperature. Unit cell parameters of the anatase phase estimated from the $d_{200}$ reflection of a=b=3.78 Å were in accordance with the literature (a=b=3.78 Å).[62]

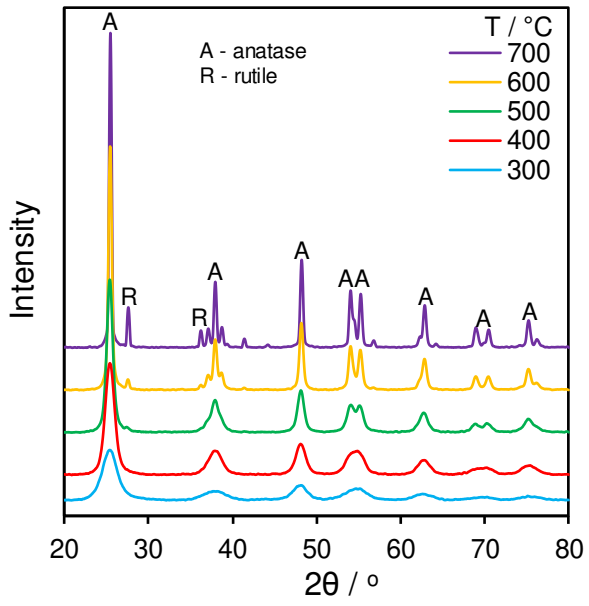


**Fig. 1.** Powder X-ray patterns of meso-$TiO_2$ as a function of calcination temperature.

Textural properties were evaluated by $N_2$ porosimetry (**Fig. 2a**), and revealed Type IV isotherms for all samples, characteristic of mesoporous materials with H2 type hysteresis loops indicating either restricted pore entrance (ink bottle shape) or an irregular channel structure of a mesopore framework.[63] The decrease in the hysteresis loop size and concomitant shift towards higher relative pressure with increasing calcination temperature evidence a progressive loss of mesoporosity, although hysteresis can still be clearly observed for the 700 °C calcined meso-$TiO_2$ sample. Sintering and a fall in mesopore volume with calcination temperature, were accompanied by a decrease in the BET surface area from 313 $m^2.g^{-1}$ for the 300 °C sample to only 19 $m^2.g^{-1}$ for meso-$TiO_2$-700C. TPO shows that the 300 °C calcined meso-$TiO_2$ had a high area despite retention of significant carbon from the F127 template within the mesopores (whose complete combustion required calcination ≥400 °C, **Fig. S1**). Samples calcined between 300-500 °C exhibited narrow BJH mesopore size distributions (**Fig. 2b**), with higher temperatures expanding and broadening mesopores. Structural changes ≥600 °C coincide with loss of both a well-defined $d_{10}$ low angle XRD reflection, and hexagonal close-packed mesopore channels observed by HRTEM (**Fig. 3**). collectively the data indicate that nanocrystallite sintering induces the gradual collapse of ordered mesopores and coincident formation of large intraparticle voids. Mesopore diameters and anatase crystallite diameters of the 400 °C calcined meso-$TiO_2$ from HRTEM were in good agreement with values from porosimetry and wide angle XRD.

**Table 1.** Physicochemical properties of meso-$TiO_2$

| Calcination temperature / °C | BET area[a] / $m^2.g^{-1}$ | Mesopore size[b] / nm | Mesopore volume[b] / $g.cm^{-3}$ | $TiO_2$ phase[c] | Crystallite size[c] / nm | Band gap[d] / eV | Mass loss[e] / % |
|---|---|---|---|---|---|---|---|
| 300 | 313 | 4.6 | 0.41 | Anatase | 5 | - | 20 (5) |
| 400 | 194 | 5.4 | 0.34 | Anatase | 7 | 3.07 | 6 (3) |
| 500 | 126 | 6.5 | 0.28 | 97 % Anatase /3 % Rutile | 11 (29) | 3.02 | 3 (2) |
| 600 | 51 | 9.7 | 0.15 | 96 %Anatase /4 % Rutile | 20 (35) | 2.97 | 1 (1) |
| 700 | 19 | 16.0 | 0.11 | 85 % Anatase /15 % Rutile | 31 (46) | 2.94 | 0 |

[a]$N_2$ BET, [b]BJH, [c]XRD (rutile values in parentheses), [d]DRUVS, [e]TPO (mass loss between 150-350 °C in parentheses).

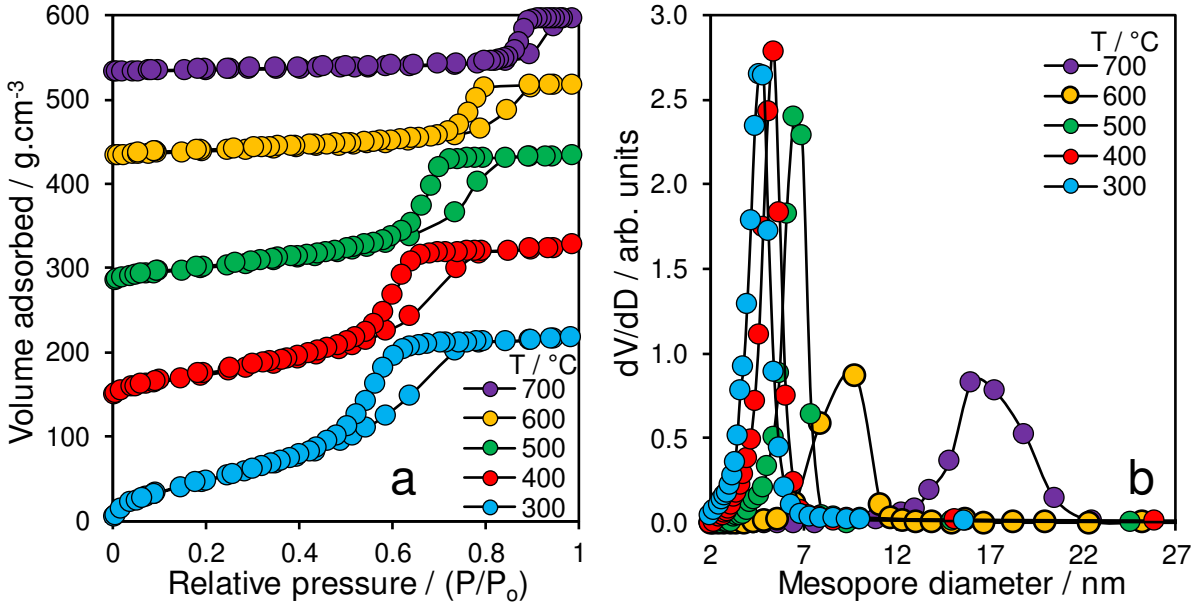


**Fig. 2.** (a) $N_2$ adsorption-desorption isotherms, and (b) corresponding BJH pore size distributions of meso-$TiO_2$ as a function of calcination temperature. Note that isotherms are offset for clarity.

DRUV spectra (**Fig. S2**) and associated Tauc plots (considering all materials as indirect band gap semiconductors due to the dominance of anatase) shown in **Fig. 4** demonstrate a strong trend between calcination temperature and optical properties of the meso-$TiO_2$ family. Besides the 300 °C sample, whose dark brown colour (due to ~15 wt% residual carbon) conferred strong UV-Vis absorption, meso-$TiO_2$ samples exhibited distinct absorption band edges between 350-415 nm which shifted to visible wavelengths with increasing calcination temperature. Corresponding optical band gaps (**Table 1**) decreased from 3.07 eV (400 °C) to 2.94 eV (700 °C) consistent with the coincident anatase→rutile phase transition.

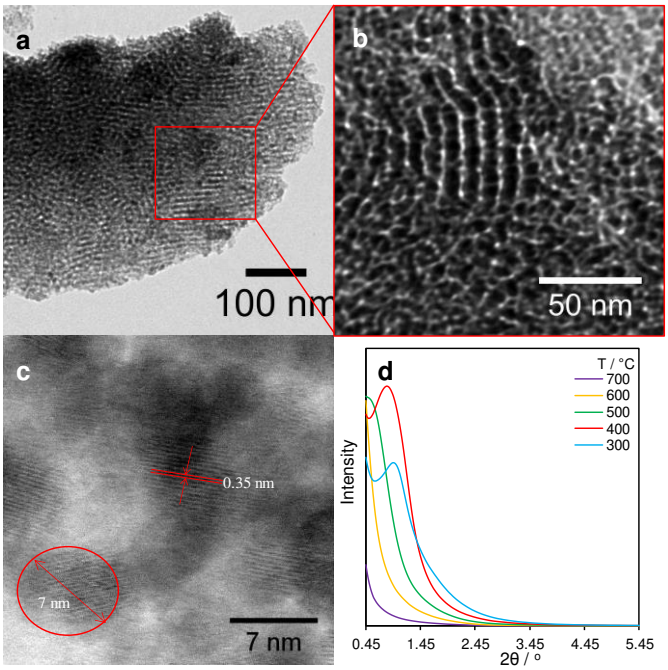


**Fig. 3.** (a-c) HRTEM images of 400 °C calcined meso-$TiO_2$, and (d) low angle XRD patterns of meso-$TiO_2$ as a function of calcination temperature.

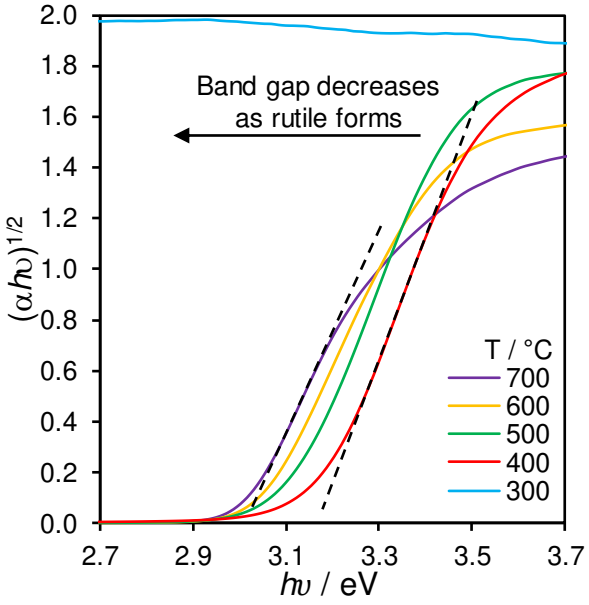


**Fig. 4.** Tauc plots of meso-$TiO_2$ as a function of calcination temperature.

***Photocatalytic Methyl Orange depollution***

Photocatalytic activity of meso-$TiO_2$ materials was subsequently evaluated for Methyl Orange (MO) degradation under UV-Vis irradiation (**Fig. 5**). It is important to recognise that Azo-dyes (exemplified by MO) are integral to the textile industry, and major sources of waste water contamination,[47] and hence their removal from aquatic environments is critical to improve human health. In the present work, dye degradation was investigated to target the removal of a specific Azo-dye commonly discharged to waste water in developing countries, and not simply to assay the general photocatalytic performance of our materials (Rochkind and co-workers published a recent critical review on this distinction [64]).

Prior to illumination, samples were stirred in the dark for 1 h to equilibrate MO adsorption: around 15 % of the initial dissolved MO adsorbed over the 300 °C calcined meso-$TiO_2$, with only ~3 % adsorbing over the other materials, and reaction data presented are corrected to discount this contribution. Negligible MO photolysis was observed over 5 h in the absence of titania. All meso-$TiO_2$ samples were active for MO photocatalytic degradation under UV-vis irradiation, with mass normalised initial rates increasing monotonically with calcination temperature (**Fig. 5b**). A plot of ln [MO] versus time reveals a linear dependence (**Fig. S3**) with a common rate constant $k_{avg}$=-0.0115 $min^{-1}$, characteristic of first order rate kinetics.[65, 66] Four distinct mechanisms are proposed for MO catalytic degradation over titania; a direct hole oxidation process[67] (**Equation 1**), hydroxyl radical oxidation[68, 69] (**Equations 2-4**), superoxide radical formation[70] (**Equations 5-9**) and ultra-fast direct electron injection into adsorbed MO[68] (**Equation 10**):

$$h_{VB}^{+} + \text{dye} \rightarrow \text{dye}^{\bullet+} \rightarrow \text{dye oxidation products} \quad (1)$$

$$h_{VB}^{+} + H_2O \rightarrow H^{+} + OH^{\cdot} \quad (2)$$

$$h_{VB}^{+} + OH^{-} \rightarrow OH^{\cdot} \quad (3)$$

$$OH^{\cdot} + \text{dye} \rightarrow \text{dye oxidation products} \quad (4)$$

$$e_{CB}^{-} + O_2 \rightarrow O_2^{\cdot-} \quad (5)$$

$$O_2^{\cdot-} + H_2O \rightarrow HO_2^{\cdot} + OH^{-} \quad (6)$$

$$HO_2^{\cdot} + H_2O \rightarrow H_2O_2 + OH^{\cdot} \quad (7)$$

$$H_2O_2 \rightarrow 2OH^{\cdot} \quad (8)$$

$$OH^{\cdot} + \text{dye} \rightarrow \text{oxidation of the dye} \quad (9)$$

$$e_{CB}^{-} + \text{dye} \rightarrow \text{degradation of the dye} \quad (10)$$

The pH of the reaction mixture rose slightly from 5.2 to 5.7 after 4 h reaction, consistent with hydroxyl radical generation during irradiation.

Since calcination simultaneously alters the structural and optical properties of mesoporous titanias, it is difficult to unequivocally identify the origin of the rate enhancement, with **Fig. 5c** evidencing a direct relationship between mesopore diameter and MO degradation, and concomitant inverse relationship with band gap. The former may be readily understood in terms of improved mass transport of the bulky dye into the mesopore network through Knudsen diffusion, for which the diffusion coefficient is proportional to pore diameter. However, the relatively weak dependence of this correlation suggests that MO (with a molecular diameter of 1.3 nm) can readily access even the smallest 5 nm mesopores.[71, 72] The far stronger rate dependence on band gap may simply reflect an exponential increase in (UV) photon absorption, or improved photoexcited charge transport and/or suppressed charge carrier recombination. **Table 2** (**Fig. S4**) shows time-resolved photoluminescence data for meso-$TiO_2$ and P25 (whose anatase:rutile composition is closest to the 700 °C calcined sample). The average radiative lifetime ($\tau_{average}$) is fitted to arise from two separate components, designated $\tau_1$ and $\tau_2$. $\tau_{average}$ increases with calcination temperature as a result of the increase in $\tau_2$ (attributed to radiative relaxation processes originating from the indirect formation of self-trapped excitons) and therefore the overall increase in the average radiative lifetime is likely due to improved charge separation across a type-II, staggered anatase/rutile heterojunction interface.[73, 74] High-resolution TEM is required to directly visualise such a heterojunction,[75] however this is extremely challenging for our mesoporous titanias, which only contain <15 % rutile randomly dispersed in a non-uniform matrix. It is important to note that activities were unchanged under pure UV irradiation (<400 nm), *indicating a negligible role for dye sensitisation in the photocatalytic mechanism* (MO adsorbs strongly in the visible region, **Fig. S5**).[64, 76] Calcination >700 °C induced additional crystallite sintering (60-140 nm) and collapse of the mesopore framework, accompanied by an almost complete loss in photoactivity. HPLC analysis identified trace succinic and malic acid as reactively-formed intermediates during the first 2 h reaction, with fumaric acid the sole organic decomposition product after 4 h (**Figure S6**), equating to ~80 % mineralisation over the meso-$TiO_2$-500C photocatalyst.

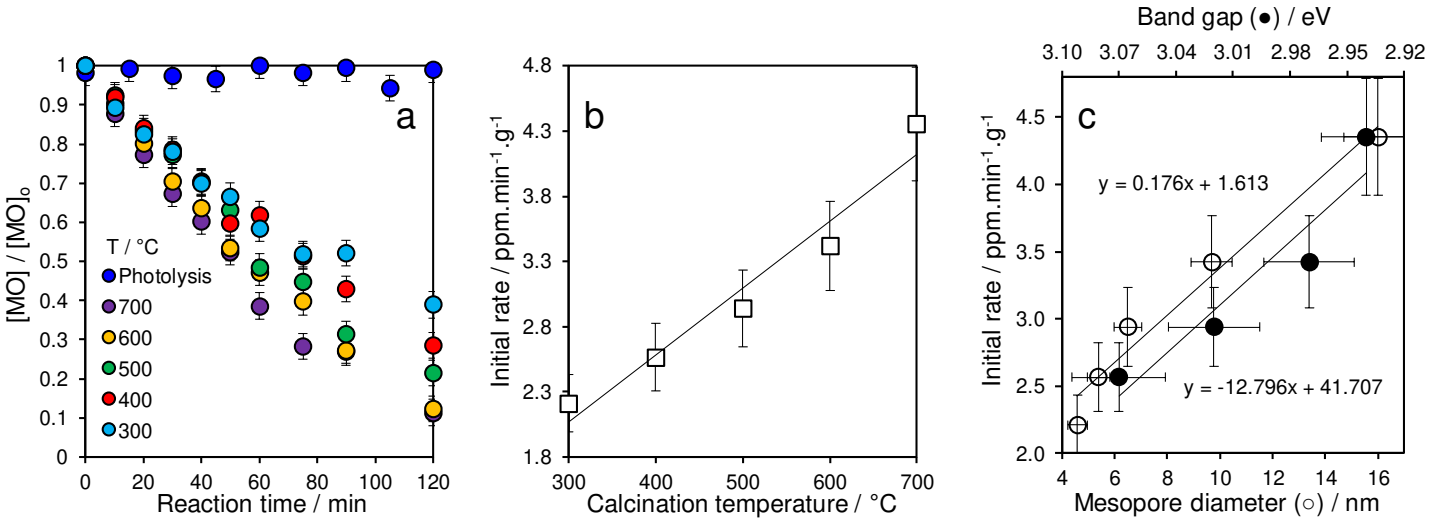


**Fig. 5.** (a) Reaction profiles for MO degradation, and corresponding initial rates of MO degradation as a function of (b) calcination temperature, and (c) mesopore diameter/band gap of meso-$TiO_2$.

**Table 2.** Time-resolved photoluminescence spectroscopy fitted parameters[a] for meso-$TiO_2$ and reference materials

| Sample | $\tau_1$ / ns | $B_1$ (%) | $\tau_2$ / ns | $B_2$ (%) | $\tau_{average}$ / ns | $\chi^2$ |
|---|---|---|---|---|---|---|
| 400[b,c] | 2.2 | 595 (83%) | 8.5 | 121 (17%) | 5.0 | 1.10 |
| 500 [b,c] | 1.4 | 2435 (98%) | 22.6 | 35 (2%) | 5.4 | 1.10 |
| 700 [b,c] | 2.2 | 381 (83%) | 17.0 | 76 (17%) | 11.2 | 1.10 |
| P25[b-d] | 1.0 | 3190 (83%) | 2.6 | 610 (83%) | 1.5 | 1.17 |
| 0.02 wt% Cu/meso-$TiO_2$-500C[b,d] | 5.6 | 2328 | 0 | - | 5.6 | 1.19 |
| CuO[b,e] | 3.5 | 1019 | 0 | - | 3.5 | 1.15 |

[a]Parameters $\tau_1$ and $\tau_2$ are the calculated lifetimes of the two contributors to the radiative lifetime. $B_1$ and $B_2$ express the relative contribution of each component to the weighted average lifetime, $\tau_{average}$. Goodness of fit between model and recorded data express by $\chi_2$ being close to unity. [b]380 nm excitation, [c]470 nm emission, [d]420 nm emission, [e]530 nm emission.

***Photocatalytic $H_2$ production***

Calcination of meso-$TiO_2$ exerted a similar effect on photocatalytic hydrogen production from water splitting under UV-Vis irradiation to that observed for MO degradation (**Figure 6**); $H_2$ productivity increased almost linearly with calcination temperature up to 700 °C. However, in this instance mesopore expansion cannot be responsible for the (dramatic) 25-fold rate-enhancement observed, since chemical mass transport of water will never be rate-limiting in aqueous solution. Rather, the increase in $H_2$ productivity with calcination temperature, which mirrors the concomitant decrease in band gap, must arise from the phase transition from anatase→rutile (quantified in **Table 1**). As discussed above for MO degradation, this phase transition is expected to result in a type-II staggered semiconductor heterojunction, thereby increasing charge carrier lifetimes and hence activity for any photocatalytic process. Furthermore, it is important to recall that the energetic position of the conduction band minimum (CBM) should be more negative than the reduction potential of water (−0.41 V vs SHE at pH 7) to produce $H_2$ ($2H^+ + 2e^- \rightarrow H_2$).[77] Recent hybrid quantum chemical calculations and high-resolution XPS on titania nanostructures[74] and electrochemical Mott-Schottky analysis[78] reveals that the rutile CBM lies 0.2-0.4 eV more negative than that of anatase (typically ~-0.4-0.65 eV vs SHE[79]). Rutile formation on meso-$TiO_2$ calcination will thus also provide a stronger thermodynamic driving force for $H_2$ evolution.

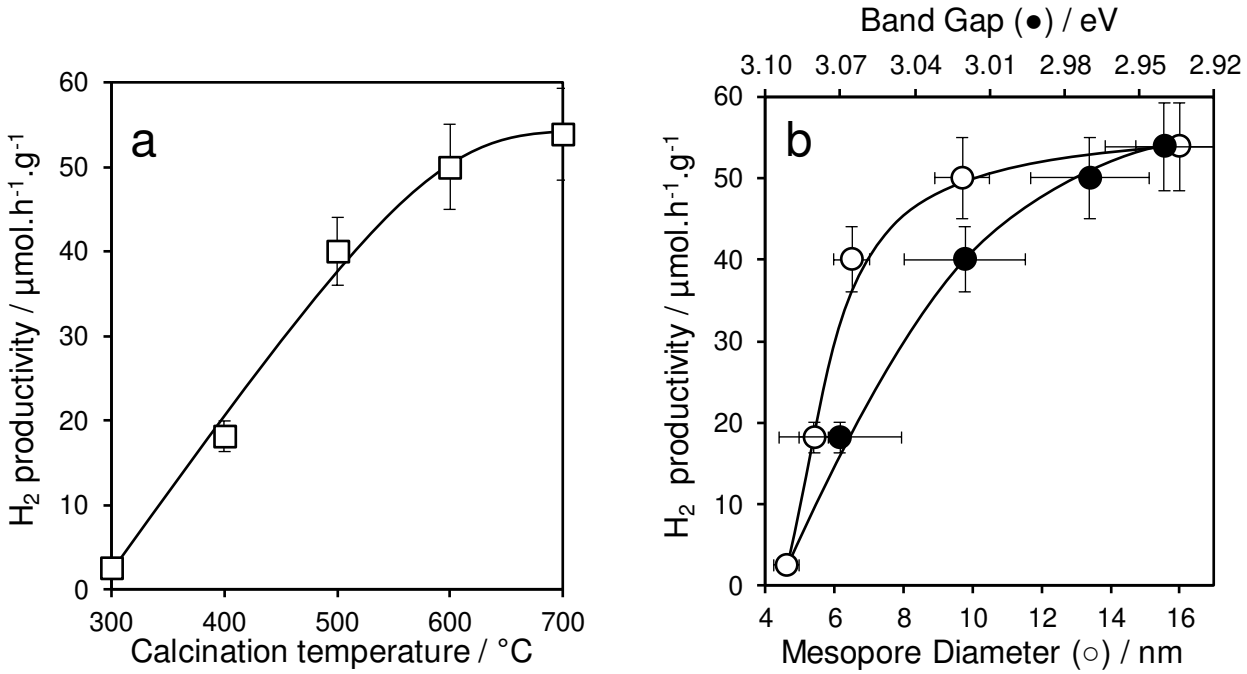


**Fig. 6.** $H_2$ production as a function of (a) calcination temperature, and (b) mesopore diameter/band gap of meso-$TiO_2$.

***Cu functionalised mesoporous $TiO_2$***

The impact of Cu deposition on the structural and photocatalytic properties of the preceding meso-$TiO_2$-500C was subsequently investigated; this support offering the optimal trade-off between textural properties and rutile content (**Table 1**), the latter desirable for heterojunction formation and enhanced photoactivity. Porosimetry evidenced minimal change in textural properties of the titania following post-synthesis functionalisation by copper at loadings between 0.02-12.33 wt% (**Table S1** and **Fig. S7a**): surface areas, mean mesopore diameters and mesopore volumes remained close to the parent meso-$TiO_2$ values demonstrating retention of the mesopore framework.

Wide angle XRD of the Cu/meso-$TiO_2$ materials (**Fig. S7b**) showed only pure anatase reflections for copper loadings between 0.02 and 8.34 wt%, with additional weak peaks at 35.7, 38.6 ° associated with (-111)/(002), (111)/(200) reflections characteristic of tenerite CuO crystallites (JCPDS card no. 45-0937) with a volume averaged diameter of 34 nm. Neither the anatase unit cell (a=b=3.78 Å) or crystallite size (11 nm) were changed following copper addition (**Table S1**), indicating that the latter was located predominantly extra-framework.

DRUVS spectra (**Fig. 7a**) and corresponding Tauc plots (**Fig. 7b**) demonstrate a systematic evolution in optical properties of the parent meso-$TiO_2$ with Cu functionalisation: the band gap absorption edge progressively increased from 350→430 nm with increasing Cu loading; this was accompanied by increased absorption between 400-600 nm possibly due to interface states arising from charge transfer between $TiO_2$ and Cu(I)/Cu(II) species, and the emergence of a new absorption band spanning 580-900 nm associated with d-d transitions in CuO[80] emerges for loadings ≥0.3 wt%. These

changes are reflected in a systematic decrease in the band gap from 3.00 eV for the parent titania to only 1.10 eV for the 12.33 wt% Cu sample (**Table S1**), consistent with the formation of bulk CuO[81] in accordance with XRD.

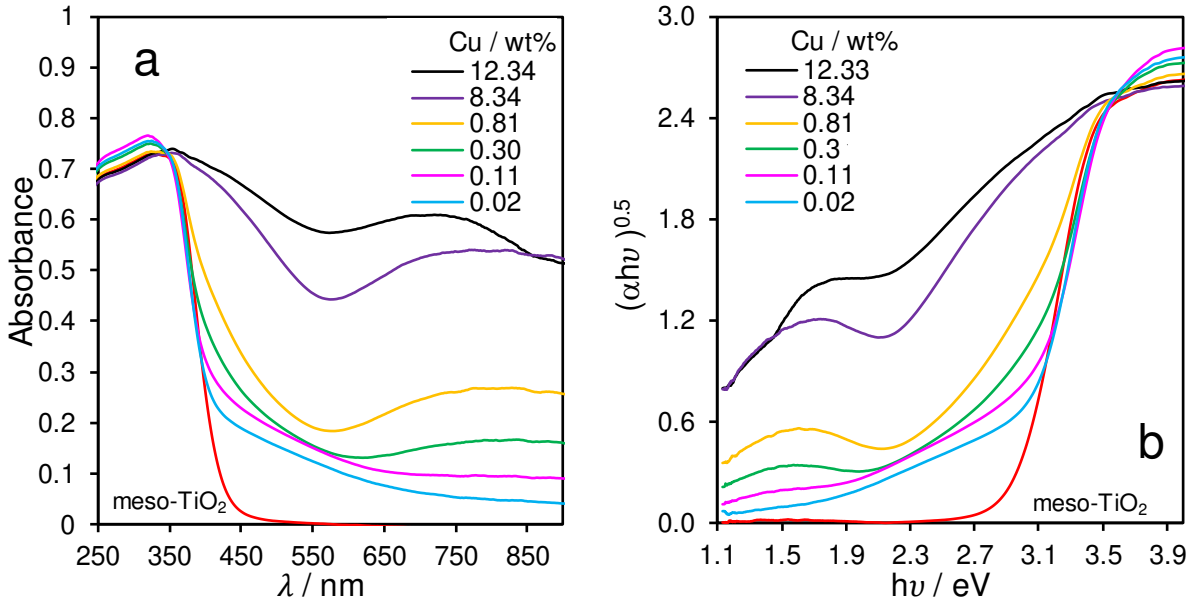


**Fig. 7.** DRUV spectra and corresponding Tauc plots of Cu/meso-$TiO_2$-500C as a function of Cu loading.

Copper co-catalysts may promote $TiO_2$ by various means, including trapping of charge carriers at the semiconductor surface and/or electron injection into the titania conduction band by metallic nanoparticles,[82-84] heterojunction formation between discrete copper oxide and titania nanoparticles,[85, 86] or framework substitution of copper cations accompanied by band energy modification and/or improved charge transport.[87, 88]

Identification of the copper chemical environment within the Cu/meso-$TiO_2$ series is thus critical to interpreting their photocatalytic performance. However, the extremely low Cu loading within some samples, and similar binding energies of Cu 2p metal and (I) oxide photoemission features, prohibits their quantification and discrimination by laboratory X-ray sources.[89] Hence the local chemical environment and oxidation state of Cu species was probed by Cu K-edge XAS. Background subtracted, normalised XANES spectra of the 0.02-12.33 wt% Cu/meso-$TiO_2$ series and $Cu_2O$, CuO and nitrate references are shown in **Fig. 8a-b**. The copper local environment evolves from that reminiscent of the Cu(II) nitrate trihydrate complex to that of bulk CuO with increasing Cu loading, with spectra exhibiting three distinct features: a weak pre-edge feature around 8977 eV, a strong rising-edge feature around 8986 eV, and an intense white line around 8996; these are attributed to dipole-forbidden 1s→3d (not observed for Cu(I) species), 1s→4$p_z$ (or 4px,ypz for Cu(I) species) and 1s→4p (continuum) transitions respectively. Least squares spectral fitting to Cu, $Cu_2O$, CuO and $Cu(NO_3)_2$ references suggested only Cu(II) were present in all Cu/meso-$TiO_2$ samples (**Fig. S8**) with loadings ≥0.81 wt% a good fit to CuO, and those <0.3 wt% an excellent fit to a mononuclear copper species. However, **Fig. 8b** reveals that the pre-edge feature characteristic of Cu(II) only emerges for Cu loadings ≥0.3 wt%, and hence copper atoms in the ultra-dilute Cu/meso-$TiO_2$ materials appear electronically similar to Cu(I) but structurally similar to those in mononuclear

complexes. Fitting of the corresponding EXAFS spectra of the 0.1 wt% Cu/meso-$TiO_2$ sample (**Fig. S9**) revealed only Cu-O scatterers around 1.94 Å, with no Cu-Cu interatomic distances (**Table S2**), consistent with isolated Cu(I) species either within the titania framework or decorating the semiconductor surface. The Cu-O nearest neighbour coordination number of 2.5 (versus 4 for both CuO and $Cu(NO_3)_2$) for 0.1 wt% Cu/meso-$TiO_2$ is consistent with either anion vacancy formation upon framework substitution of Ti(IV) with Cu(I), or atomically-dispersed, undercoordinated Cu(I) atoms at the titania surface. Since copper was introduced by post-modification of mesoporous titania, employing a comparatively low temperature processing step, the latter scenario is more feasible. The constant band gap, and anatase lattice parameter and crystal size, following the addition of ultra-low Cu concentrations to the parent meso-$TiO_2$ supports the hypothesis that single copper atoms are dispersed over titania. Time-resolved photoluminescence of the 0.02 wt% Cu/meso-$TiO_2$ highlight a significant increase in charge carrier relaxation time $\tau_1$ relative to the parent 500 °C calcined titania upon copper functionalisation (**Table 2**), possibly due to isolated Cu(I) species acting as hole traps.

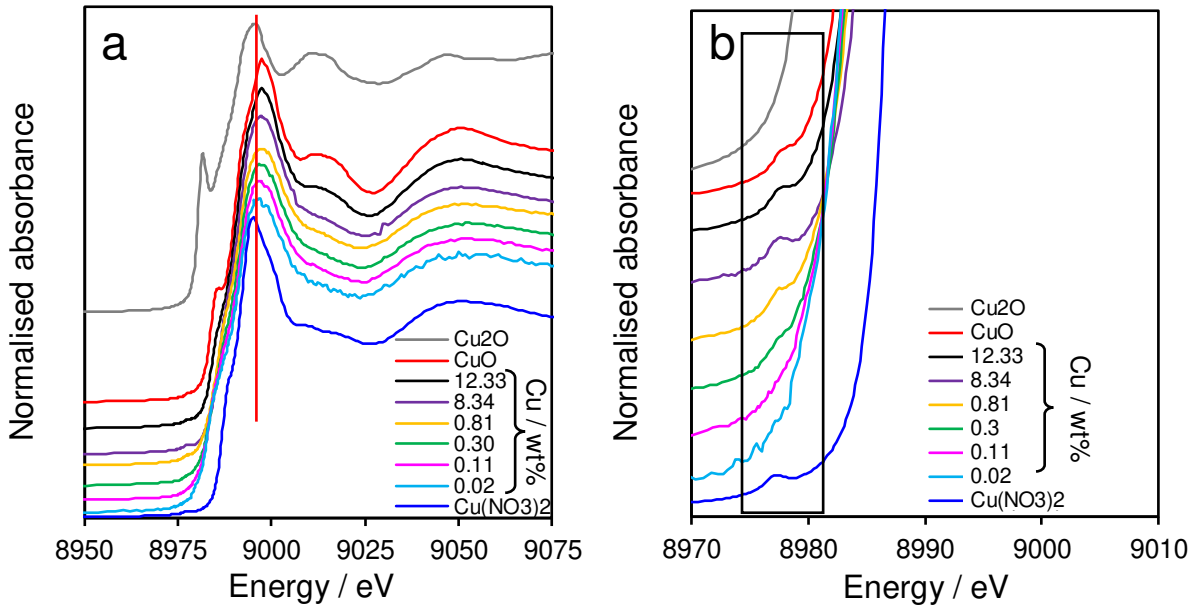


**Fig. 8.** (a-b) Cu K-edge XANES of Cu/meso-$TiO_2$-500C as a function of Cu loading.

The impact of copper on the photocatalytic performance of mesoporous titania for MO photodegradation under UV-Vis irradiation is shown in **Fig. 9**. Mass normalised initial rates of dye degradation were inversely proportional to copper loading (and bulk CuO content determined by XANES fitting), but directly proportional to the concentration of isolated Cu(I) species (from XANES). We attribute the latter relationship to the creation of oxygen vacancies upon introducing Cu(I) species into the titania framework; these oxygen vacancies likely capture photoexcited electrons to form F-centres,[90] thereby suppressing charge carrier recombination, promoting either direct hole oxidation or indirect hydroxyl oxidation mechanisms (**Equations 1** or **2-4**). Dye degradation via a hydroxyl radical mechanism (**Equation 2**) requires photoexcited holes in the valence band with energies >2.6 eV. This threshold is exceeded by the valence band maxima of all Cu/meso-$TiO_2$ catalysts (determined as ~2.72-2.95 eV from valence band spectra in **Fig. S10**), and hence MO degradation may occur via oxidation by hydroxyl radicals. For loadings above 0.81 wt% Cu, photoactivity fell to that

of the parent 500 °C calcined meso-$TiO_2$ support, indicating negligible benefits from CuO despite its impact on optical properties. The 0.02 wt% Cu/meso-$TiO_2$ catalyst also exhibited excellent stability, with negligible loss in photodegradation activity over three consecutive recycles, consistent with preservation of Cu(I) isolated sites from XANES analysis (**Fig. S11**). CuO displays poor performance as a promoter, probably due to its smaller valence band maximum relative to the meso-$TiO_2$-500C anatase parent (~2.66 eV versus 2.95 eV [91]) which offers a lower thermodynamic driving force for catalytic oxidation, and the large size of CuO nanoparticles (34 nm for 12.33 wt% Cu) and corresponding poor interfacial contact and inefficient heterojunction formation with titania. It is interesting to note that only the 12.33 wt% Cu/meso-$TiO_2$, for which crystalline CuO was observed, was active under visible light irradiation (>400 nm, 8 mW $cm^{-2}$). This confirms that Cu(I) species did not significantly modify the band gap of the titania support, and that the poor observed initial rate of only 0.244 $ppm.min^{-1}.g^{-1}$ arose solely from the visible absorbing CuO phase.

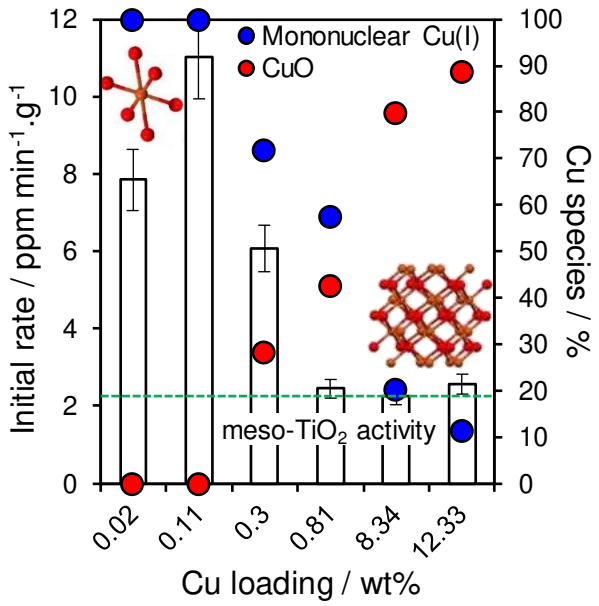


**Fig. 9.** Correlation between initial rate of photocatalytic MO degradation and Cu species (from XANES) in Cu/meso-$TiO_2$-500C. Dotted line indicates activity of parent meso-$TiO_2$-500C.

In contrast to MO degradation, photocatalytic $H_2$ production over in Cu/meso-$TiO_2$-500C exhibited a volcano dependence on copper loading (**Fig. 10**), reaching a maximum for 0.81 wt% Cu, a material comprising ~60 % mononuclear Cu(I) species and 40 % CuO. The lack of promotion at low Cu loadings, wherein only Cu(I) species exist, is understandable in terms of the preceding hypothesis that Cu(I) doping introduces F-centers into the meso-$TiO_2$ framework (which trap photoexcited electrons required for $H_2$ production). Similarly, the baseline activity of the 12.33 wt% Cu/meso-$TiO_2$-500C which is dominated by crystalline CuO is also explicable, since the CBM of CuO lies ~0.96 eV, significantly below that necessary to reduce protons,[91] and therefore cannot contribute directly to $H_2$ production as a semiconductor photocatalyst. The origin of the synergy between Cu(I) and CuO responsible for the 3-4-fold rate-enhancement observed for the 0.81 wt% Cu/meso-$TiO_2$-500C remains unclear, but highlights the impact of subtle variations in the composition of doped titania on corresponding photophysical/catalytic properties.

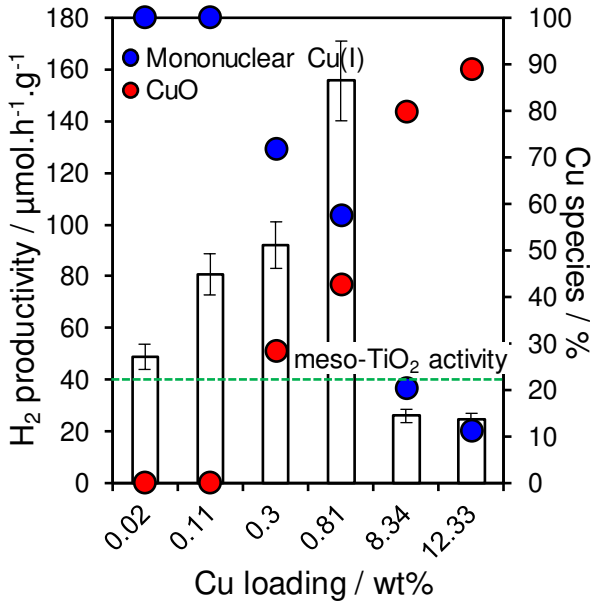


**Fig. 10.** Correlation between $H_2$ productivity and Cu species (from XANES) in Cu/meso-$TiO_2$-500C. Dotted line indicates activity of parent meso-$TiO_2$-500C.

## Conclusions

A facile route is demonstrated to high surface area, mesoporous $TiO_2$ in which the pore diameter, anatase:rutile phase composition and corresponding photophysical properties may be readily tuned through thermal processing of a surfactant-templated sol-gel, and whose performance may be dramatically enhanced through the incorporation of single atom Cu (I) species. Increasing calcination temperature from 300→700 °C induces progressive expansion of uniform mesopores from 5→16 nm respectively, and a concomitant decrease in surface area, accompanied by the transformation of smaller (11→31 nm) anatase to larger (30→46 nm) rutile nanocrystallites) and slight band gap narrowing. These structural and electronic changes strongly influence photocatalytic activity for Methyl Orange degradation under UV-Vis irradiation. Initial rates of photodegradation exhibit a weak, direct correlation with mesopore diameter and strong inverse (direct) correlation with band gap (rutile concentration), imparting a two-fold rate enhancement through high temperature calcination. Photocatalytic $H_2$ production is even more sensitive to the anatase→rutile phase transition, which confers a dramatic 25-fold increase in water splitting, likely due to a combination of heterojunction formation and the higher conduction band minimum of rutile titania. Post-functionalisation of mesoporous $TiO_2$ by wet-impregnation with ultra-low ( ≤0.1 wt%) concentrations of copper affords atomically-dispersed Cu(I) species, likely extra-framework decorating the surface of titania crystallites. Despite their high dilution, the incorporation of Cu(I) species results in a six-fold rate enhancement for Methyl Orange photodegradation relative to the unmodified (500 °C) mesoporous $TiO_2$, possibly due to the introduction of oxygen vacancies which may act as electron traps to increase charge carrier lifetimes. A synergy between Cu(I) and CuO over 0.81 wt% Cu/meso-$TiO_2$-500C increased photocatalytic $H_2$ production four-fold relative to the mesoporous anatase scaffold. The importance of tailoring both textural and photophysical properties of heterogeneous

photocatalysts to optimise chemical mass transport, and the energetics and lifetime of charge carriers, emerge as key design features.

## Acknowledgements

We thank the EPSRC (EP/K021796/1 and EP/K029525/2) for financial support.

## References

[1] S.C. Roy, O.K. Varghese, M. Paulose, C.A. Grimes, Toward Solar Fuels: Photocatalytic Conversion of Carbon Dioxide to Hydrocarbons, Acs Nano, 4 (2010) 1259-1278.
[2] D. Chen, X.G. Zhang, A.F. Lee, Synthetic strategies to nanostructured photocatalysts for CO2 reduction to solar fuels and chemicals, Journal of Materials Chemistry A, 3 (2015) 14487-14516.
[3] A. Kudo, Y. Miseki, Heterogeneous photocatalyst materials for water splitting, Chemical Society Reviews, 38 (2009) 253-278.
[4] S. Malato, P. Fernández-Ibáñez, M.I. Maldonado, J. Blanco, W. Gernjak, Decontamination and disinfection of water by solar photocatalysis: Recent overview and trends, Catalysis Today, 147 (2009) 1-59.
[5] M.N. Chong, B. Jin, C.W.K. Chow, C. Saint, Recent developments in photocatalytic water treatment technology: A review, Water Research, 44 (2010) 2997-3027.
[6] X. Chen, S.S. Mao, Titanium Dioxide Nanomaterials: Synthesis, Properties, Modifications, and Applications, Chemical Reviews, 107 (2007) 2891-2959.
[7] R.I. Bickley, T. Gonzalez-Carreno, J.S. Lees, L. Palmisano, R.J.D. Tilley, A structural investigation of titanium dioxide photocatalysts, Journal of Solid State Chemistry, 92 (1991) 178-190.
[8] D.C. Hurum, A.G. Agrios, K.A. Gray, T. Rajh, M.C. Thurnauer, Explaining the Enhanced Photocatalytic Activity of Degussa P25 Mixed-Phase TiO2 Using EPR, The Journal of Physical Chemistry B, 107 (2003) 4545-4549.
[9] R. Daghrir, P. Drogui, D. Robert, Modified TiO2 For Environmental Photocatalytic Applications: A Review, Industrial & Engineering Chemistry Research, 52 (2013) 3581-3599.
[10] E.J.W. Crossland, N. Noel, V. Sivaram, T. Leijtens, J.A. Alexander-Webber, H.J. Snaith, Mesoporous TiO2 single crystals delivering enhanced mobility and optoelectronic device performance, Nature, 495 (2013) 215-219.
[11] D.M. Antonelli, J.Y. Ying, Synthesis of Hexagonally Packed Mesoporous TiO2 by a Modified Sol–Gel Method, Angewandte Chemie International Edition in English, 34 (1995) 2014-2017.
[12] C.K. Tsung, J. Fan, N.F. Zheng, Q.H. Shi, A.J. Forman, J.F. Wang, G.D. Stucky, A General Route to Diverse Mesoporous Metal Oxide Submicrospheres with Highly Crystalline Frameworks, Angewandte Chemie-International Edition, 47 (2008) 8682-8686.
[13] W. Zhou, F.F. Sun, K. Pan, G.H. Tian, B.J. Jiang, Z.Y. Ren, C.G. Tian, H.G. Fu, Well-Ordered Large-Pore Mesoporous Anatase TiO2 with Remarkably High Thermal Stability and Improved Crystallinity: Preparation, Characterization, and Photocatalytic Performance, Advanced Functional Materials, 21 (2011) 1922-1930.
[14] M.F. Atitar, A.A. Ismail, S.A. Al-Sayari, D. Bahnemann, D. Afanasev, A.V. Emeline, Mesoporous TiO2 nanocrystals as efficient photocatalysts: Impact of calcination temperature and phase transformation on photocatalytic performance, Chemical Engineering Journal, 264 (2015) 417-424.
[15] W. Li, Z.X. Wu, J.X. Wang, A.A. Elzatahry, D.Y. Zhao, A Perspective on Mesoporous TiO2 Materials, Chem. Mat., 26 (2014) 287-298.
[16] R. Zhang, A.A. Elzatahry, S.S. Al-Deyab, D. Zhao, Mesoporous titania: From synthesis to application, Nano Today, 7 (2012) 344-366.
[17] A.A. Ismail, D.W. Bahnemann, Mesoporous titania photocatalysts: preparation, characterization and reaction mechanisms, Journal of Materials Chemistry, 21 (2011) 11686-11707.
[18] U.I. Gaya, A.H. Abdullah, Heterogeneous photocatalytic degradation of organic contaminants over titanium dioxide: A review of fundamentals, progress and problems, Journal of Photochemistry and Photobiology C-Photochemistry Reviews, 9 (2008) 1-12.

[19] J. Schneider, M. Matsuoka, M. Takeuchi, J.L. Zhang, Y. Horiuchi, M. Anpo, D.W. Bahnemann, Understanding TiO2 Photocatalysis: Mechanisms and Materials, Chemical Reviews, 114 (2014) 9919-9986.
[20] A. Selloni, Crystal growth: Anatase shows its reactive side, Nat Mater, 7 (2008) 613-615.
[21] N. Serpone, Is the band gap of pristine TiO2 narrowed by anion- and cation-doping of titanium dioxide in second-generation photocatalysts?, Journal of Physical Chemistry B, 110 (2006) 24287-24293.
[22] M.C. Yan, F. Chen, J.L. Zhang, M. Anpo, Preparation of controllable crystalline titania and study on the photocatalytic properties, Journal of Physical Chemistry B, 109 (2005) 8673-8678.
[23] D.C. Hurum, A.G. Agrios, K.A. Gray, T. Rajh, M.C. Thurnauer, Explaining the enhanced photocatalytic activity of Degussa P25 mixed-phase TiO2 using EPR, Journal of Physical Chemistry B, 107 (2003) 4545-4549.
[24] X.Q. Gong, A. Selloni, Reactivity of anatase TiO2 nanoparticles: The role of the minority (001) surface, Journal of Physical Chemistry B, 109 (2005) 19560-19562.
[25] A. Vittadini, A. Selloni, F.P. Rotzinger, M. Gratzel, Structure and energetics of water adsorbed at TiO2 anatase (101) and (001) surfaces, Physical Review Letters, 81 (1998) 2954-2957.
[26] L.J. Liu, H.L. Zhao, J.M. Andino, Y. Li, Photocatalytic CO2 Reduction with H2O on TiO2 Nanocrystals: Comparison of Anatase, Rutile, and Brookite Polymorphs and Exploration of Surface Chemistry, Acs Catalysis, 2 (2012) 1817-1828.
[27] C.B. Almquist, P. Biswas, Role of synthesis method and particle size of nanostructured TiO(2) on its photoactivity, Journal of Catalysis, 212 (2002) 145-156.
[28] L.X. Yang, S.L. Luo, Y. Li, Y. Xiao, Q. Kang, Q.Y. Cai, High Efficient Photocatalytic Degradation of p-Nitrophenol on a Unique Cu2O/TiO2 p-n Heterojunction Network Catalyst, Environmental Science & Technology, 44 (2010) 7641-7646.
[29] Y. Cong, J.L. Zhang, F. Chen, M. Anpo, Synthesis and characterization of nitrogen-doped TiO2 nanophotocatalyst with high visible light activity, Journal of Physical Chemistry C, 111 (2007) 6976-6982.
[30] N.P. Xu, Z.F. Shi, Y.Q. Fan, J.H. Dong, J. Shi, M.Z.C. Hu, Effects of particle size of TiO2 on photocatalytic degradation of methylene blue in aqueous suspensions, Industrial & Engineering Chemistry Research, 38 (1999) 373-379.
[31] M. Kong, Y.Z. Li, X. Chen, T.T. Tian, P.F. Fang, F. Zheng, X.J. Zhao, Tuning the Relative Concentration Ratio of Bulk Defects to Surface Defects in TiO2 Nanocrystals Leads to High Photocatalytic Efficiency, Journal of the American Chemical Society, 133 (2011) 16414-16417.
[32] W.J. Ong, L.L. Tan, S.P. Chai, S.T. Yong, A.R. Mohamed, Facet- Dependent Photocatalytic Properties of TiO2-Based Composites for Energy Conversion and Environmental Remediation, Chemsuschem, 7 (2014) 690-719.
[33] Y.L. Yu, P. Zhang, L.M. Guo, Z.D. Chen, Q. Wu, Y.H. Ding, W.J. Zheng, Y. Cao, The Design of TiO2 Nanostructures (Nanoparticle, Nanotube, and Nanosheet) and Their Photocatalytic Activity, Journal of Physical Chemistry C, 118 (2014) 12727-12733.
[34] P. Sangpour, F. Hashemi, A.Z. Moshfegh, Photoenhanced Degradation of Methylene Blue on Cosputtered M:TiO2 (M = Au, Ag, Cu) Nanocomposite Systems: A Comparative Study, Journal of Physical Chemistry C, 114 (2010) 13955-13961.
[35] X.Q. Qiu, M. Miyauchi, K. Sunada, M. Minoshima, M. Liu, Y. Lu, D. Li, Y. Shimodaira, Y. Hosogi, Y. Kuroda, K. Hashimoto, Hybrid CuxO/TiO2 Nanocomposites As Risk-Reduction Materials in Indoor Environments, Acs Nano, 6 (2012) 1609-1618.
[36] G. Colon, M. Maicu, M.C. Hidalgo, J.A. Navio, Cu-doped TiO2 systems with improved photocatalytic activity, Applied Catalysis B-Environmental, 67 (2006) 41-51.
[37] D. Liu, Y. Fernández, O. Ola, S. Mackintosh, M. Maroto-Valer, C.M.A. Parlett, A.F. Lee, J.C.S. Wu, On the impact of Cu dispersion on CO2 photoreduction over Cu/TiO2, Catalysis Communications, 25 (2012) 78-82.
[38] J.G. Yu, J.R. Ran, Facile preparation and enhanced photocatalytic H-2-production activity of Cu(OH)(2) cluster modified TiO2, Energy & Environmental Science, 4 (2011) 1364-1371.
[39] Y. Liu, B. Zhang, L. Luo, X. Chen, Z. Wang, E. Wu, D. Su, W. Huang, TiO2/Cu2O Core/Ultrathin Shell Nanorods as Efficient and Stable Photocatalysts for Water Reduction, Angewandte Chemie International Edition, 54 (2015) 15260-15265.
[40] Z. Wang, D. Brouri, S. Casale, L. Delannoy, C. Louis, Exploration of the preparation of Cu/TiO2 catalysts by deposition–precipitation with urea for selective hydrogenation of unsaturated hydrocarbons, Journal of Catalysis, 340 (2016) 95-106.

[41] S. Obregón, M.J. Muñoz-Batista, M. Fernández-García, A. Kubacka, G. Colón, Cu–TiO2 systems for the photocatalytic H2 production: Influence of structural and surface support features, Applied Catalysis B: Environmental, 179 (2015) 468-478.
[42] Y. Wang, W. Duan, B. Liu, X. Chen, F. Yang, J. Guo, The Effects of Doping Copper and Mesoporous Structure on Photocatalytic Properties of TiO2, Journal of Nanomaterials, 2014 (2014) 7.
[43] World Health Organization WHO (2017), Global Health Observatory Data Repository, WHO, World Health Organization, 2016.
[44] S.D. Richardson, T.A. Ternes, Water Analysis: Emerging Contaminants and Current Issues, Analytical Chemistry, 86 (2014) 2813-2848.
[45] T. Deblonde, C. Cossu-Leguille, P. Hartemann, Emerging pollutants in wastewater: A review of the literature, International Journal of Hygiene and Environmental Health, 214 (2011) 442-448.
[46] Y.J. Chan, M.F. Chong, C.L. Law, D.G. Hassell, A review on anaerobic–aerobic treatment of industrial and municipal wastewater, Chemical Engineering Journal, 155 (2009) 1-18.
[47] F.M.D. Chequer, G.A.R.d. Oliveira, E.R.A.c. Ferraz, J.C. Cardoso, M.V.B. Zanoni, D.P.d. Oliveira, Textile Dyes: Dyeing Process and Environmental Impact, in: M. Günay (Ed.) Eco-Friendly Textile Dyeing and Finishing, InTech, Rijeka, 2013, pp. Ch. 06.
[48] S. Karthikeyana, M.P. Pachamuthu, M.A. Isaacs, S. Kumar, A.F. Lee, G. Sekaran, Cu and Fe oxides dispersed on SBA-15: A Fenton type bimetallic catalyst for N,N-diethyl-p-phenyl diamine degradation, Applied Catalysis B-Environmental, 199 (2016) 323-330.
[49] F. Persico, M. Sansotera, C.L. Bianchi, C. Cavallotti, W. Navarrini, Photocatalytic activity of TiO2-embedded fluorinated transparent coating for oxidation of hydrosoluble pollutants in turbid suspensions, Applied Catalysis B-Environmental, 170 (2015) 83-89.
[50] W.-K. Jo, S. Kumar, M.A. Isaacs, A.F. Lee, S. Karthikeyan, Cobalt promoted TiO2/GO for the photocatalytic degradation of oxytetracycline and Congo Red, Applied Catalysis B: Environmental, 201 (2017) 159-168.
[51] F.F. Dias, A.A.S. Oliveira, A.P. Arcanjo, F.C.C. Moura, J.G.A. Pacheco, Residue-based iron catalyst for the degradation of textile dye via heterogeneous photo-Fenton, Applied Catalysis B-Environmental, 186 (2016) 136-142.
[52] G. Ovejero, A. Rodriguez, A. Vallet, J. Garcia, Catalytic wet air oxidation of a non-azo dye with Ni/MgAlO catalyst, Chemical Engineering Journal, 215 (2013) 168-173.
[53] Y.M. Liu, S. Chen, X. Quan, H.T. Yu, H.M. Zhao, Y.B. Zhang, Efficient Mineralization of Perfluorooctanoate by Electro-Fenton with H2O2 Electro-generated on Hierarchically Porous Carbon, Environmental Science & Technology, 49 (2015) 13528-13533.
[54] P.V. Nidheesh, R. Gandhimathi, Trends in electro-Fenton process for water and wastewater treatment: An overview, Desalination, 299 (2012) 1-15.
[55] C.A. Cole, L.D. Ochs, F.C. Funnell, Hydrogen Peroxide as a Supplemental Oxygen Source, Journal (Water Pollution Control Federation), 46 (1974) 2579-2592.
[56] Q. Yang, H. Choi, S.R. Al-Abed, D.D. Dionysiou, Iron-cobalt mixed oxide nanocatalysts: Heterogeneous peroxymonosulfate activation, cobalt leaching, and ferromagnetic properties for environmental applications, Applied Catalysis B-Environmental, 88 (2009) 462-469.
[57] N. Armaroli, V. Balzani, The Future of Energy Supply: Challenges and Opportunities, Angewandte Chemie International Edition, 46 (2007) 52-66.
[58] T. Faunce, S. Styring, M.R. Wasielewski, G.W. Brudvig, A.W. Rutherford, J. Messinger, A.F. Lee, C.L. Hill, H. deGroot, M. Fontecave, D.R. MacFarlane, B. Hankamer, D.G. Nocera, D.M. Tiede, H. Dau, W. Hillier, L. Wang, R. Amal, Artificial photosynthesis as a frontier technology for energy sustainability, Energy & Environmental Science, 6 (2013) 1074-1076.
[59] X. Chen, S. Shen, L. Guo, S.S. Mao, Semiconductor-based Photocatalytic Hydrogen Generation, Chemical Reviews, 110 (2010) 6503-6570.
[60] R.A. Spurr, H. Myers, Quantitative Analysis of Anatase-Rutile Mixtures with an X-Ray Diffractometer, Analytical Chemistry, 29 (1957) 760-762.
[61] S. Bakardjieva, J. Šubrt, V. Štengl, M.J. Dianez, M.J. Sayagues, Photoactivity of anatase–rutile TiO2 nanocrystalline mixtures obtained by heat treatment of homogeneously precipitated anatase, Applied Catalysis B: Environmental, 58 (2005) 193-202.
[62] Anatase: Anatase mineral information and data, 2017.

[63] F. Rouquerol, J. Rouquerol, K.S.W. Sing, Adsorption by Powders and Porous Solids: Principles, Methodology and Applications, Academic Press1999.
[64] M. Rochkind, S. Pasternak, Y. Paz, Using Dyes for Evaluating Photocatalytic Properties: A Critical Review, Molecules, 20 (2015) 88.
[65] X.H. Wang, J.G. Li, H. Kamiyama, Y. Moriyoshi, T. Ishigaki, Wavelength-sensitive photocatalytic degradation of methyl orange in aqueous suspension over iron(III)-doped TiO2 nanopowders under UV and visible light irradiation, Journal of Physical Chemistry B, 110 (2006) 6804-6809.
[66] D.S. Tsoukleris, A.I. Kontos, P. Aloupogiannis, P. Falaras, Photocatalytic properties of screen-printed titania, Catalysis Today, 124 (2007) 110-117.
[67] E. Neyens, J. Baeyens, A review of classic Fenton's peroxidation as an advanced oxidation technique, Journal of Hazardous Materials, 98 (2003) 33-50.
[68] L.H. Yu, J.Y. Xi, M.D. Li, H.T. Chan, T. Su, D.L. Phillips, W.K. Chan, The degradation mechanism of methyl orange under photo-catalysis of TiO2, Physical Chemistry Chemical Physics, 14 (2012) 3589-3595.
[69] S.K. Kansal, M. Singh, D. Sud, Studies on photodegradation of two commercial dyes in aqueous phase using different photocatalysts, Journal of Hazardous Materials, 141 (2007) 581-590.
[70] S. Kumar, C.M.A. Parlett, M.A. Isaacs, D.V. Jowett, R.E. Douthwaite, M.C.R. Cockett, A.F. Lee, Facile synthesis of hierarchical Cu2O nanocubes as visible light photocatalysts, Applied Catalysis B-Environmental, 189 (2016) 226-232.
[71] J. Goscianska, M. Marciniak, R. Pietrzak, Mesoporous carbons modified with lanthanum(III) chloride for methyl orange adsorption, Chemical Engineering Journal, 247 (2014) 258-264.
[72] F. Gritti, G. Guiochon, The quantitative impact of the mesopore size on the mass transfer mechanism of the new 1.9 µm fully porous Titan-C18 particles. I: Analysis of small molecules, Journal of Chromatography A, 1384 (2015) 76-87.
[73] B. Vijayan, N.M. Dimitrijevic, T. Rajh, K. Gray, Effect of Calcination Temperature on the Photocatalytic Reduction and Oxidation Processes of Hydrothermally Synthesized Titania Nanotubes, The Journal of Physical Chemistry C, 114 (2010) 12994-13002.
[74] D.O. Scanlon, C.W. Dunnill, J. Buckeridge, S.A. Shevlin, A.J. Logsdail, S.M. Woodley, C.R.A. Catlow, M.J. Powell, R.G. Palgrave, I.P. Parkin, G.W. Watson, T.W. Keal, P. Sherwood, A. Walsh, A.A. Sokol, Band alignment of rutile and anatase TiO2, Nat Mater, 12 (2013) 798-801.
[75] A. Kafizas, X. Wang, S.R. Pendlebury, P. Barnes, M. Ling, C. Sotelo-Vazquez, R. Quesada-Cabrera, C. Li, I.P. Parkin, J.R. Durrant, Where Do Photogenerated Holes Go in Anatase:Rutile TiO2? A Transient Absorption Spectroscopy Study of Charge Transfer and Lifetime, The Journal of Physical Chemistry A, 120 (2016) 715-723.
[76] N. Barbero, D. Vione, Why Dyes Should Not Be Used to Test the Photocatalytic Activity of Semiconductor Oxides, Environmental Science & Technology, 50 (2016) 2130-2131.
[77] A. Fujishima, T.N. Rao, D.A. Tryk, Titanium dioxide photocatalysis, Journal of Photochemistry and Photobiology C: Photochemistry Reviews, 1 (2000) 1-21.
[78] Y. Nosaka, A.Y. Nosaka, Reconsideration of Intrinsic Band Alignments within Anatase and Rutile TiO2, The Journal of Physical Chemistry Letters, 7 (2016) 431-434.
[79] A. Iacomino, G. Cantele, F. Trani, D. Ninno, DFT Study on Anatase TiO2 Nanowires: Structure and Electronic Properties As Functions of Size, Surface Termination, and Morphology, The Journal of Physical Chemistry C, 114 (2010) 12389-12400.
[80] Y.Q. Wang, T.T. Jiang, D.W. Meng, J.H. Kong, H.X. Jia, M.H. Yu, Controllable fabrication of nanostructured copper compound on a Cu substrate by a one-step route, Rsc Advances, 5 (2015) 16277-16283.
[81] B. Bhushan, Handbook of nanomaterials properties, 2014.
[82] J.Z.Y. Tan, Y. Fernández, D. Liu, M. Maroto-Valer, J. Bian, X. Zhang, Photoreduction of CO2 using copper-decorated TiO2 nanorod films with localized surface plasmon behavior, Chemical Physics Letters, 531 (2012) 149-154.
[83] S. Zhang, B. Peng, S. Yang, H. Wang, H. Yu, Y. Fang, F. Peng, Non-noble metal copper nanoparticles-decorated TiO2 nanotube arrays with plasmon-enhanced photocatalytic hydrogen evolution under visible light, International Journal of Hydrogen Energy, 40 (2015) 303-310.
[84] L.S. Yoong, F.K. Chong, B.K. Dutta, Development of copper-doped TiO2 photocatalyst for hydrogen production under visible light, Energy, 34 (2009) 1652-1661.
[85] S. Qin, F. Xin, Y. Liu, X. Yin, W. Ma, Photocatalytic reduction of CO2 in methanol to methyl formate over CuO–TiO2 composite catalysts, Journal of Colloid and Interface Science, 356 (2011) 257-261.
[86] S. Xu, A.J. Du, J. Liu, J. Ng, D.D. Sun, Highly efficient CuO incorporated TiO2 nanotube photocatalyst for hydrogen production from water, International Journal of Hydrogen Energy, 36 (2011) 6560-6568.

[87] Y. Lee, S. Kim, J.K. Kang, S.M. Cohen, Photocatalytic CO2 reduction by a mixed metal (Zr/Ti), mixed ligand metal-organic framework under visible light irradiation, Chemical Communications, 51 (2015) 5735-5738.
[88] A. Dhakshinamoorthy, A.M. Asiri, H. Garcia, Metal-Organic Framework (MOF) Compounds: Photocatalysts for Redox Reactions and Solar Fuel Production, Angewandte Chemie-International Edition, 55 (2016) 5414-5445.
[89] NIST X-ray Photoelectron Spectroscopy (XPS) Database, Version 3.5, 2017.
[90] B. Choudhury, M. Dey, A. Choudhury, Shallow and deep trap emission and luminescence quenching of TiO2 nanoparticles on Cu doping, Applied Nanoscience, 4 (2014) 499-506.
[91] V.J. Babu, S. Vempati, T. Uyar, S. Ramakrishna, Review of one-dimensional and two-dimensional nanostructured materials for hydrogen generation, Physical Chemistry Chemical Physics, 17 (2015) 2960-2986.